PHYSICAL REVIEW FLUIDS **6**, 013103 (2021)

Fluid dynamics and efficiency of colonial swimming via multijet propulsion at intermediate Reynolds numbers

Houshuo Jiang,[1,*] John H. Costello,[2,3] and Sean P. Colin[2,4]
[1] *Department of Applied Ocean Physics and Engineering, Woods Hole Oceanographic Institution, Woods Hole, Massachusetts 02543, USA*
[2] *Whitman Center, Marine Biological Laboratory, Woods Hole, Massachusetts 02543, USA*
[3] *Department of Biology, Providence College, Providence, Rhode Island 02918, USA*
[4] *Department of Marine Biology and Environmental Science, Roger Williams University, Bristol, Rhode Island 02809, USA*

(Received 23 July 2020; revised 29 October 2020; accepted 24 December 2020; published 22 January 2021)

Colonial physonect siphonophores swim via laterally distributed multijet propulsion at intermediate Reynolds numbers (Re's) on the orders of 1–1000. Here, a computational fluid dynamics approach that assumes steady axisymmetric flow is employed to investigate the underlying fluid mechanics and adaptive values of colonial swimming via laterally distributed multijet propulsion, with comparison with rear-jetting single-jet propulsion. Results show that imposed flow fields, drag coefficients, powers, and efficiencies all vary significantly depending upon Re, jet angle, and way of jetting. For a given Re, two types of optimal jet angles are determined: one in the range of 61°–70° that maximizes the quasipropulsive efficiency (i.e., to minimize the jet power), and another in the range of 34°–45° that maximizes the Froude propulsion efficiency (i.e., to minimize the wake). Comparison with values for a documented siphonophore, *Nanomia bijuga*, indicates that siphonophores rely upon a spectrum of jet angles between these two theoretical optima. Multiple, laterally directed jets produced by colonial forms are less energetically efficient for propulsion than single, posteriorly directed jets produced by solitary individuals; however, colonial swimming achieves energetic benefits for jetting individuals within the colony because they require significantly lower per-module power than that required by a lone jet module swimming at the same speed. Hence, by sharing propulsive duties, colony formation helps alleviate inherent power constraints that characterize cnidarian muscles. Importantly, multiple jets that are directed obliquely away from the central body axis exert less impact on other colony members within the siphosome that is towed in the wake of the jetting aggregation.

DOI: 10.1103/PhysRevFluids.6.013103

I. INTRODUCTION

Jet propulsion has evolved multiple times independently in the history of life and may have been the earliest truly macroscopic mode of animal locomotion [1]. Quite a number of marine animals use jet propulsion, including pelagic tunicates [2–4] [Fig. 1(a)], cnidarian medusae [5–9] [Fig. 1(b)], scallops [10,11] [Fig. 1(c)], and cephalopod molluscs, e.g., *Nautilus* [12–14] [Fig. 1(d)] and squid [15–20] [Fig. 1(e)]. Despite their morphological diversity, these animals share generally a similar plan for jet propulsion, whereby thrust is generated by ejecting fluid from a single nozzle or

---

[*] hsjiang@whoi.edu

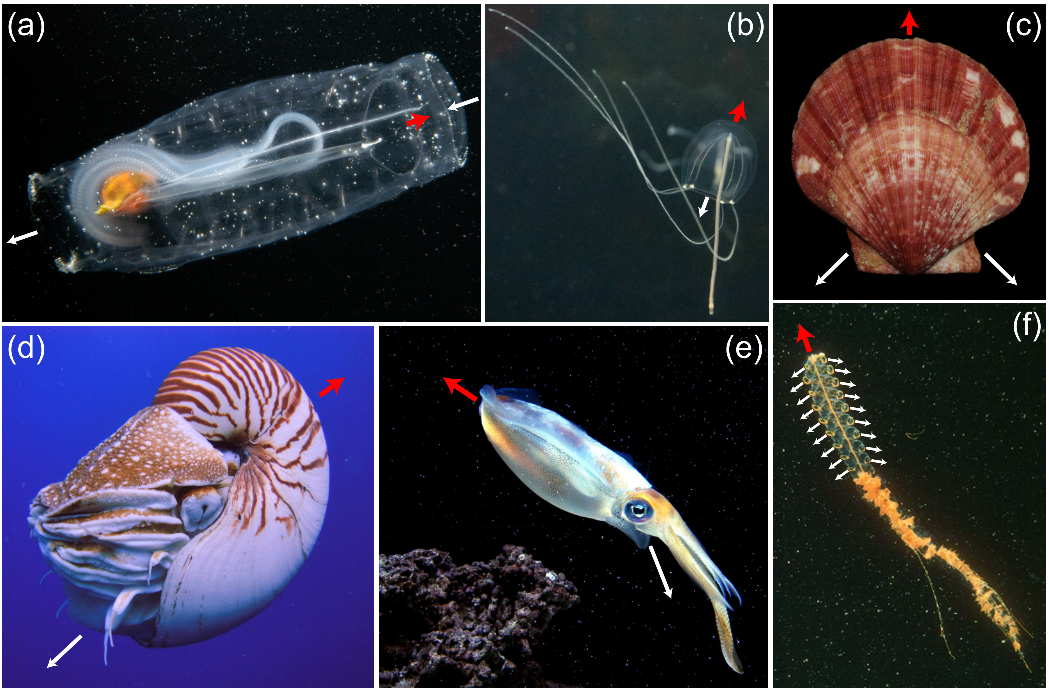

FIG. 1. Jet propulsion animals: (a) the salp *Salpa thompsoni* solitary, by Laurence Madin, ©Woods Hole Oceanographic Institution (with permission), (b) the hydromedusa *Sarsia tubulosa*, licensed under CC BY 2.0, (c) the queen scallop *Chlamys opercularis*, by Merlin Charon, licensed under CC0, (d) the Palau *Nautilus belauensis*, by Manuae, licensed under CC BY-SA 3.0, (e) the bigfin reef squid *Sepioteuthis lessoniana*, by George Berninger Jr., licensed under CC BY-SA 3.0, and (f) the physonect siphonophore *Marrus orthocanna*, Credit: NOAA. In each picture, the red arrow indicates the swimming direction, while the white arrow(s) the jet direction(s) [also the intake flow direction in (a)].

opening to achieve body motion in the opposite direction, i.e., single-jet propulsion (Videos 1 and 2 of Supplemental Material [21]). (A slight exception is that the scallop jet propulsion involves two isolated, seemingly noninteracting backward jets [Fig. 1(c)].)

In contrast to the single-jet propulsion, one animal group, the physonect siphonophores, has achieved multijet propulsion with extraordinary sophistication [22–25] [Fig. 1(f)] (Video 3 of Supplemental Material [21]). Physonect siphonophores are colony-forming cnidarians that are highly successful and widespread in the world's oceans; they are important predators in pelagic ecosystems, feeding pervasively on prey ranging from zooplankton nauplii to small fish [26,27]. Among them, *Nanomia bijuga* is the most abundant and documented physonect species. During active swimming, the whole body of an *N. bijuga* colony [Fig. 2(a)] is propelled through water by a multijet propulsive column less than 4 cm in length, called the nectosome. The nectosome is arranged linearly from genetically identical clones that are jet-producing locomotory modules called nectophores. Individual nectophores issue jets that are distributed along the lateral surface of the nectosome; these jets produce thrust and torque that control the swimming speed and direction of the whole colony, i.e., laterally distributed multijet propulsion [23]. The nectosome pulls feeding and reproductive colony members, arranged within a portion of the colony termed the siphosome. The whole colony can migrate daily several hundred meters through different water layers.

The fluid dynamics of multijet propulsion in aquatic animals remains largely unexplored except for a few simplified theoretical and observational studies focusing on specific aspects (e.g., in Refs. [28,24,25]). A more systematic fluid-dynamic investigation is needed for achieving

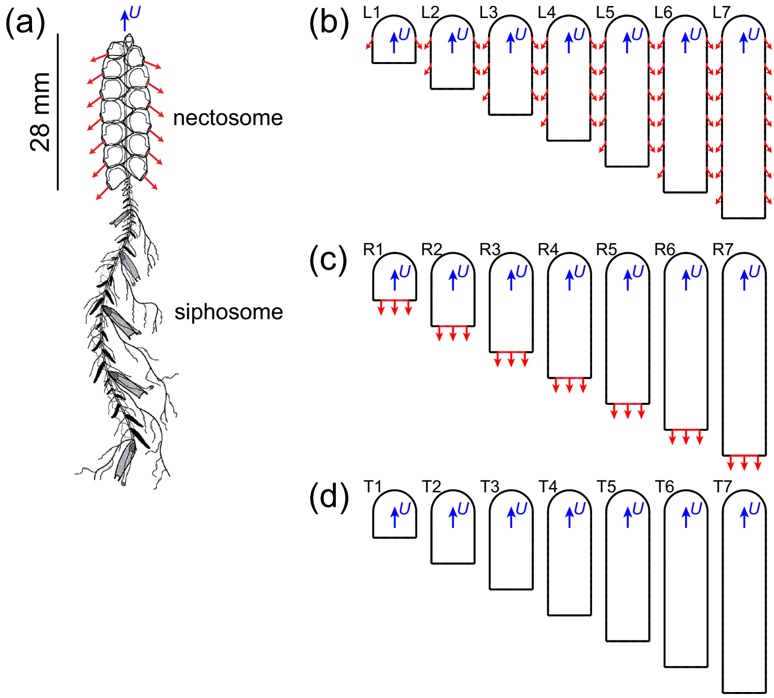

FIG. 2. (a) General body structure of the physonect *N. bijuga*, modified from a video-recorded sequence depicted in Fig. 2 of Ref. [23], where the whole colony swims forward at a speed U (the blue arrow) while being propelled by the laterally distributed multijets (the red arrows). Schematics of three CFD-simulated propulsion strategies: a self-propelled axisymmetric body swimming steadily via the laterally distributed multijet propulsion, where 1–7 jet modules are considered [(b) L1–L7]; a self-propelled axisymmetric body swimming steadily via the rear-jetting single-jet propulsion, where seven different body lengths respectively equal to those of the L1–L7 bodies are considered [(c) R1–R7]; and a towed axisymmetric body, where seven different body lengths respectively equal to those of the L1–L7 bodies are considered [(d) T1–T7].

mechanistic understanding of the adaptive values of colonial swimming via multijet propulsion. For example, with regard to swimming and propulsion, cnidarian swimmers are energy limited because they typically have much greater water content, having much lower body carbon and muscle mass per unit body volume than squid, fish, and crustaceans [2,29–32]. Colonial swimming via multijet propulsion in physonect siphonophores may be adaptive for optimizing the use of energy, yet the mechanics allowing this are undescribed. A fluid-dynamic investigation can inform this issue by comparing energy use of solitary and colonial jet production. The laterally distributed multijet propulsion in colonial siphonophores has two important fluid-dynamic aspects. First, colonial siphonophores swim within the intermediate regime of the Reynolds number ($\mathrm{Re} = UL/\nu$, where U is the swimming speed, L is the nectosome length, and ν is the kinematic viscosity of seawater), i.e., on the order of 1–1000. In this regime, drag coefficients vary significantly with Re by 2–3 orders of magnitude. Consequently, mechanical powers and efficiencies for swimming and propulsion vary strongly with Re (i.e., with the swimming speed and the body length or number of jet modules). Second, in the laterally distributed multijet propulsion, the lateral jets significantly alter the laminar boundary-layer flow along the nectosome's lateral surface, thereby directly affecting the viscous drag. (An early flow visualization investigation has demonstrated that a blowing jet can significantly alter the laminar boundary layer along an airfoil profile (Fig. 16 of Ref. [33]). Also, a great number of previous studies have been dedicated to the interaction between jets and crossflow boundary layers at high Reynolds number and supersonic regimes [34,35].) Thus, the drag coefficients, mechanical powers, and swimming efficiencies all depend strongly on jet angles that modulate the interaction between the lateral jets and the boundary-layer flow, and there exist optimal jet angles that maximize swimming efficiencies for given Re's. This contrasts sharply with the single-jet propulsion, where the rear-jetting single jet does not interact directly with the lateral boundary-layer flow but alters overwhelmingly the pressure distribution around the jet opening, thereby directly affecting the pressure drag. Thus, the laterally distributed multijet propulsion and the rear-jetting single-jet propulsion have distinctly different variation patterns for swimming efficiencies.

In order to shed light on the adaptive values of colonial swimming via multijet propulsion and elucidate the underlying fluid-dynamic principles, the present study uses a computational fluid dynamics (CFD) approach to simulate the flow imposed by a self-propelled axisymmetric body that swims steadily via the laterally distributed multijet propulsion. A trial and error iteration method is used to achieve the balance between total jet thrust and body drag, i.e., self-propelled steady swimming. Considering the interaction between the laterally distributed multijets and the laminar boundary-layer flow along the lateral surface of the axisymmetric body, no simple analytical expressions for drag coefficients as functions of Re are available; however, the CFD approach can effectively evaluate this issue. A large number of parametric simulations have been carried out to investigate how drag coefficients, mechanical powers, and swimming efficiencies vary with the jet angle and with Re (i.e., with the swimming speed and the body length or number of jet modules). For the purpose of comparison, similar simulations have also been performed for cases of a self-propelled axisymmetric body that swims steadily via the rear-jetting single-jet propulsion and of a towed axisymmetric body. Previous studies used CFD to simulate the flow fields imposed by jet-propelled swimming animals [36–42], but all focused on the rear-jetting single-jet propulsion. The present study is a CFD investigation of animal swimming via the laterally distributed multijet propulsion at intermediate Reynolds numbers and a fluid-dynamic comparison between swimming via the laterally distributed multijet propulsion and swimming via the rear-jetting single-jet propulsion.

II. NUMERICAL SIMULATION METHOD

A. CFD-simulated propulsion strategies

Three propulsion strategies are considered, including two real-world jet-propulsion strategies. First, a self-propelled axisymmetric body swims steadily via the laterally distributed multijet propulsion [Fig. 2(b)], similar to an *N. bijuga* colony [Fig. 2(a)]. Seven bodies respectively consisting of 1–7 jet modules are constructed, starting from the jet module comprising a hemispherical head of a radius 3.85 mm and a unit cylindrical column of a base radius 3.85 mm and a height of 4.62 mm, and by subsequently adding the unit cylindrical columns [Fig. 2(b): L1–L7]. Each unit cylindrical column has a jet opening of a width 0.77 mm, located along the frontmost edge of the lateral surface of the unit. The body dimensions closely resemble those of the video-recorded *N. bijuga* colony depicted in Fig. 2 of Ref. [23]. Second, a self-propelled axisymmetric body swims steadily via the rear-jetting single-jet propulsion [Fig. 2(c)]. Seven bodies are constructed, with body lengths respectively equal to those of the L1–L7 bodies [Fig. 2(c): R1–R7]. The rear-end surface of each body has a jet opening of an area equal to the laterally located jet area of the L1 body. Third, an axisymmetric body is towed steadily [Fig. 2(d)]. Again, seven bodies are constructed, with body lengths respectively equal to those of the L1–L7 bodies [Fig. 2(d): T1–T7].

B. Computational domain and boundary conditions

The axisymmetric body is considered to move steadily along its axisymmetry axis at intermediate Reynolds numbers (i.e., on the order of 1–1000); therefore, the imposed flow is assumed laminar, steady, and axisymmetric. As a result, only a meridian plane is included as the computational domain. A cylindrical polar coordinate system is adopted with the axisymmetry axis of the body taken as the axial x axis and r being the radial distance from the x axis [Fig. 3(a)].

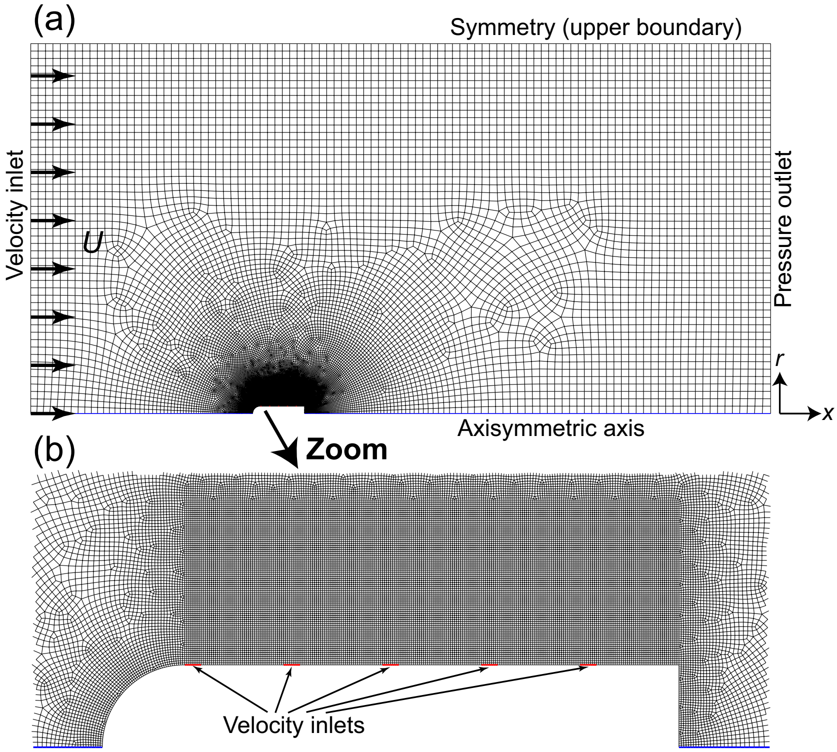

FIG. 3. Grid and boundary conditions for the axisymmetric CFD model: (a) the whole computational domain; (b) the near-body region.

The computational domain is $100R$ in the x direction and $50R$ in the r direction [Fig. 3(a)], where $R(=3.85\,\mathrm{mm})$ is the cross-sectional radius of the axisymmetric body. The domain is discretized into ~51 300 quadrilateral control volumes (CVs) whose sizes are stretched radially outward at a constant rate of 1.04 from the axisymmetric body to the domain boundaries. A symmetry boundary condition is specified on the upper boundary. A pressure-outlet boundary condition is specified on the right boundary. A velocity-inlet boundary condition of a rightward velocity U is imposed on the left boundary to model the axisymmetric body swimming leftward at the speed U, whereas the axisymmetric body itself is set as a stationary wall boundary condition. The jet openings along the surface of the axisymmetric body are prescribed as velocity-inlet boundary conditions to model the propulsive jets of given jet angles and speeds [Fig. 3(b)].

C. Numerical solver specifications

The laminar, steady, and axisymmetric flow field around the steadily moving axisymmetric body is governed by the steady incompressible Navier-Stokes equations together with the continuity equation (not shown for brevity). To obtain the flow field, these equations under the above-described boundary conditions are numerically solved by using the commercially available, unstructured, finite-volume CFD software package ANSYS FLUENT (version 18.1.0). Throughout this study, the fluid density ρ is $1.0237 \times 10^3\,\mathrm{kg/m^3}$ and the fluid kinematic viscosity ν is $1.184 \times 10^{-6}\,\mathrm{m^2/s}$; both are the values for seawater with salinity 32 at 15 °C at one normal atmosphere. The mass density of the axisymmetric body is assumed to be equal to the fluid density. As to the numerical schemes, the highly accurate third-order MUSCL (Monotone Upstream-Centered Schemes for Conservation Laws) scheme is used for spatial interpolation. The PRESTO! (PREssure STaggering

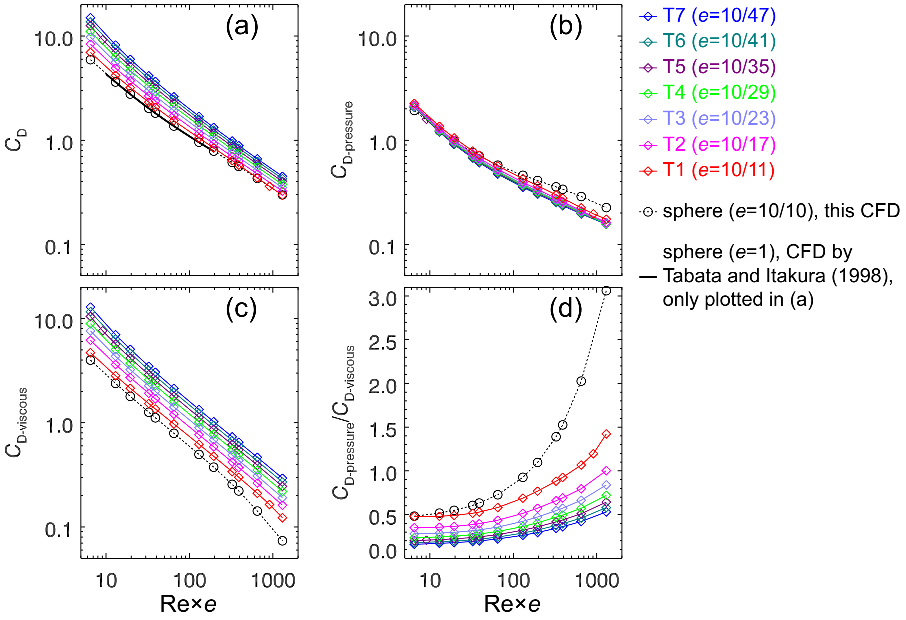

FIG. 4. CFD-simulated drag coefficients C_D (a), pressure drag coefficients $C_{D\text{-pressure}}$ (b), viscous drag coefficients $C_{D\text{-viscous}}$ (c), and $C_{D\text{-pressure}}/C_{D\text{-viscous}}$ (d) plotted as functions of Re × e, for a steadily towed sphere and for seven steadily towed axisymmetric bodies, T1–T7, of sequentially decreasing aspect ratios e. Re × e is the Reynolds number that is defined based on the cross-sectional diameter. Given the same cross-sectional diameter, increasing Re × e is equivalent to increasing the towing velocity.

Option) scheme is selected as the pressure interpolation scheme. The PISO (Pressure-Implicit with Splitting of Operators) scheme is used for pressure-velocity coupling.

For the two jet-propulsion strategies considered, a trial and error iteration method is used to achieve the balance between total jet thrust T and body drag D, i.e., self-propelled steady swimming. Specifically, a shell script involving a loop is used to realize the iteration method in the following steps: (1) For a given swimming velocity U, a trial value of the jet speed U_{jet} is chosen initially, and both U and U_{jet} are stored as input parameters in an input file for ANSYS FLUENT; (2) ANSYS FLUENT reads the input file, computes a flow field, and outputs a text file that holds body drag D; [Note that ANSYS FLUENT calculates D as the axial component of the area integral of pressure and shear stress over the body surface, and that the present study has validated the accuracy of ANSYS FLUENT's drag calculation by simulating flow around a sphere for intermediate Re's and comparing the resulted drag coefficients with known data (see Fig. 4 below)]; (3) A FORTRAN utility program reads D from the text file, calculates a new U_{jet} by forcing $T = D$ and using the equation that relates T to U_{jet} (see Sec. II D below), and updates U_{jet} in the input file for ANSYS FLUENT; and (4) Steps 2–4 are repeated until $D = T$ is achieved under a prescribed convergence criterion. In practice, it usually takes 20–30 iterations to end up with $D = T$ to at least seven significant digits.

D. Drag coefficients, mechanical powers, and swimming efficiencies

Drag coefficients, mechanical powers, and swimming efficiencies are computed from the simulated flow fields, for understanding the adaptive values of the laterally distributed multijet propulsion and comparing with the rear-jetting single-jet propulsion. The drag coefficient C_D is calculated as [43]

$$C_D \equiv \frac{D}{0.5\rho U^2 A_{\mathrm{cs}}} = \frac{D_{\mathrm{viscous}} + D_{\mathrm{pressure}}}{0.5\rho U^2 A_{\mathrm{cs}}}, \tag{1}$$

where $A_{\mathrm{cs}} = \pi R^2$ is the cross-sectional area of the axisymmetric body, D is body drag, D_{viscous} is viscous drag (i.e., the axial component of the area integral of shear stress over the body surface), and D_{pressure} is pressure drag (i.e., the axial component of the area integral of pressure over the body surface). Moreover, the viscous drag coefficient $C_{D\text{-viscous}}$ is calculated as

$$C_{D\text{-viscous}} \equiv \frac{D_{\mathrm{viscous}}}{0.5\rho U^2 A_{\mathrm{cs}}}, \tag{2}$$

and the pressure drag coefficient $C_{D\text{-pressure}}$ is calculated as

$$C_{D\text{-pressure}} \equiv \frac{D_{\mathrm{pressure}}}{0.5\rho U^2 A_{\mathrm{cs}}}. \tag{3}$$

For the laterally distributed multijet propulsion, the total jet thrust T_{mj} is calculated, according to the linear momentum theorem [44], as

$$T_{\mathrm{mj}} = \sum_{i=1}^{N} \left(\rho A_{\mathrm{jet}} U_{\mathrm{jet},i}^2 \sin\theta_i \cos\theta_i\right), \tag{4}$$

where N is the total number of jets, A_{jet} is the jet area of each jet, and $U_{\mathrm{jet},i}$ and θ_i are, respectively, the jet speed and angle of the i th jet in a stationary frame of reference, and the jet angle is measured from the direction opposite to swimming to the jet direction. The total jet power P_{mj} is calculated as

$$P_{\mathrm{mj}} = \sum_{i=1}^{N} \left[\rho A_{\mathrm{jet}} U_{\mathrm{jet},i} \sin\theta_i \frac{\left(U_{\mathrm{jet},i}^2 + 2UU_{\mathrm{jet},i}\cos\theta_i\right)}{2}\right]. \tag{5}$$

For the rear-jetting single-jet propulsion, the jet thrust T_{sj} is calculated as [1]

$$T_{\mathrm{sj}} = \rho A_{\mathrm{jet}} (U_{\mathrm{jet}} + U) U_{\mathrm{jet}}. \tag{6}$$

The jet power P_{sj} is calculated as

$$P_{\mathrm{sj}} = \rho A_{\mathrm{jet}} (U_{\mathrm{jet}} + U) \frac{\left(U_{\mathrm{jet}}^2 + 2UU_{\mathrm{jet}}\right)}{2}. \tag{7}$$

Two types of swimming efficiency are computed. First, the hydromechanical efficiency or Froude propulsion efficiency η_{FPE} [45] is calculated as

$$\eta_{\mathrm{FPE}} \equiv \frac{P_{\mathrm{useful}}}{P_{\mathrm{jet}}}, \tag{8}$$

where $P_{\mathrm{useful}} = DU$ is the useful mechanical power, i.e., the power needed to overcome the resisting body drag in the jet propulsion, and P_{jet} is the jet power that is calculated according to Eq. (5) for the laterally distributed multijet propulsion or Eq. (7) for the rear-jetting single-jet propulsion. For steady rear-jetting single-jet propulsion, $D = T_{\mathrm{sj}}$; substituting Eqs. (6) and (7) into Eq. (8) recovers the classical equation for the Froude propulsion efficiency [1]:

$$\eta_{\mathrm{FPE}} = \frac{2U}{(U_{\mathrm{jet}} + U) + U}, \tag{9}$$

where $U_{\mathrm{jet}} + U$ is the jet velocity relative to the jet opening.

Second, the quasipropulsive efficiency η_{QPE} [46,47] is calculated as

$$\eta_{\mathrm{QPE}} \equiv \frac{P_{\mathrm{tow}}}{P_{\mathrm{jet}}}, \tag{10}$$

where $P_{\mathrm{tow}} = D_{\mathrm{tow}}U$ is the mechanical power needed to tow the nonjetting body at the same speed U as in the jet propulsion, i.e., D_{tow} is the drag acting on the towed nonjetting body. According to Ref. [47], the quasipropulsive efficiency η_{QPE} is a rational nondimensional metric for comparing the propulsive fitness of self-propulsion mechanisms, seeking minimized mechanical power consumption under size and velocity constraints. For fish undulatory swimming and cilia-propelled swimming in protists and other organisms, the Froude propulsion efficiency η_{FPE} is ill defined because drag and thrust cannot be separated; however, for jet propulsion, both η_{QPE} and η_{FPE} are well defined for calculation.

E. CFD performance validation and grid refinement study

The performance of the CFD simulations is validated by computing the drag coefficients for a steadily towed sphere and for each of the seven steadily towed axisymmetric bodies [Fig. 2(d): T1–T7]. As shown in Fig. 4(a), the present CFD-simulated drag coefficients for the sphere compare well to those simulated previously by other researchers [48]. The seven axisymmetric bodies have the same cross-sectional radius R as the sphere but sequentially longer body lengths (=sequentially smaller aspect ratios, defined as $e = 2R/L$ where L is the body length). As a result, the curves of the drag coefficients C_D plotted for the seven bodies rise sequentially, according to decreasing aspect ratios, above the curve plotted for the sphere that has a unit aspect ratio [Fig. 4(a)]. The seven axisymmetric bodies have exactly the same front body shape and the same back body shape; therefore, the curves of the pressure drag coefficients $C_{D\text{-pressure}}$ all lie roughly on top of each other [Fig. 4(b)]. In contrast, the sphere having a different body shape experiences larger $C_{D\text{-pressure}}$ than each of the seven bodies in the range of higher $\mathrm{Re} \times e$ [Fig. 4(b)]. On the other hand, the viscous drag coefficients $C_{D\text{-viscous}}$ increase sequentially as the aspect ratio decreases from $e = 1$ for the sphere to $e = 10/47$ for the longest axisymmetric body, i.e., with increasing the surface area, for the whole range of $\mathrm{Re} \times e$ [Fig. 4(c)]. The ratios of $C_{D\text{-pressure}}/C_{D\text{-viscous}}$ increase either as $\mathrm{Re} \times e$ increases or as the aspect ratio e increases [Fig. 4(d)]. As Re decreases, the $C_{D\text{-pressure}}/C_{D\text{-viscous}}$ ratio for the sphere approaches 0.5, the value for the Stokes flow around a steadily towed sphere [Fig. 4(d)].

The grid refinement study is conducted with three grids: (1) the baseline grid that consists of ~51 300 quadrilateral CVs [Fig. 3(a)], (2) the doubled grid that consists of ~161 200 quadrilateral CVs, and (3) the halved grid that consists of ~19 600 quadrilateral CVs. All three grids have been used to simulate a video-recorded case of an *N. bijuga* colony swimming via the laterally distributed multijet propulsion. Excellent grid convergence between the baseline grid and the doubled grid is demonstrated in Fig. 5. Therefore, the baseline grid has been chosen for all other simulations.

III. RESULTS AND DISCUSSION

A. General description of the simulated flow fields

The simulated flow fields vary significantly with different propulsion strategies and Re's (Figs. 6 and 7). For example, adopting the same jet angle for all four lateral jets and swimming at 0.001 m/s, L4 maximizes its quasipropulsive efficiency at a jet angle of ~70° (see below). Here, $\mathrm{Re} = 18.9$; the streamline pattern and vorticity field of L4 [Figs. 6(a) and 6(b)] are completely different from those of R4 [Figs. 6(e) and 6(f)] and T4 [Figs. 6(i) and 6(j)]; the velocity magnitude field of L4 [Fig. 6(c)] decays spatially faster, both in front of and behind the body, than those of R4 [Fig. 6(g)] and T4 [Fig. 6(k)], but slower laterally to the body. The three pressure fields also differ significantly [Figs. 6(d), 6(h), and 6(l)] in that L4 has a prominent negative pressure zone behind the body [Fig. 6(d)] while R4 has a strong positive pressure zone associated with its rear jet [Fig. 6(h)].

Adopting the same jet angle for all four lateral jets and swimming at 0.1 m/s, L4 maximizes its quasipropulsive efficiency at a jet angle of ~64° (see below). Here, $\mathrm{Re} = 1886.1$; the streamline patterns and the vorticity, velocity magnitude, and pressure fields still differ significantly among the three propulsion strategies (Fig. 7). However, compared with $\mathrm{Re} = 18.9$, the differences almost

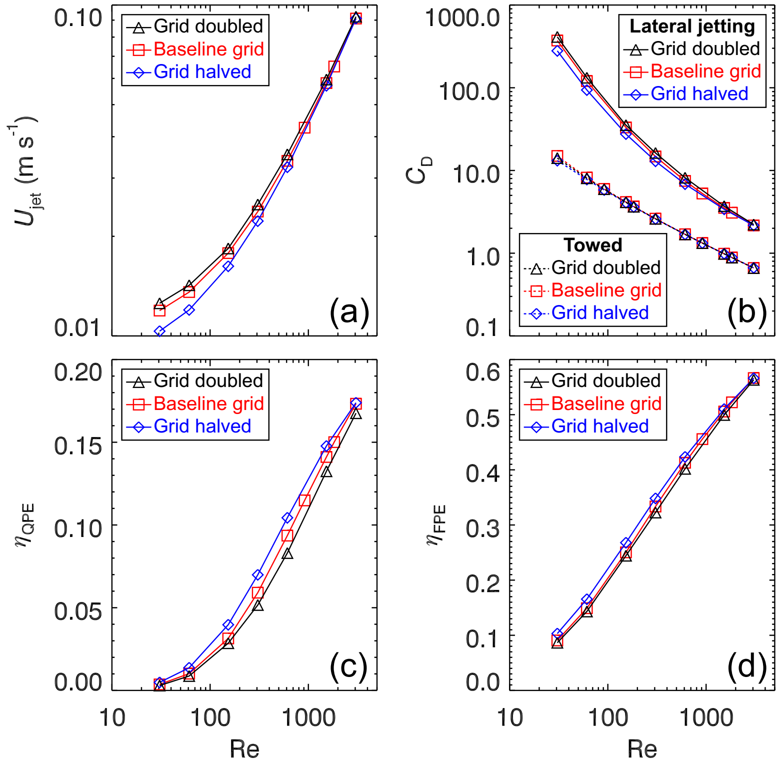

FIG. 5. Grid refinement simulations of a video-recorded swimming of an *N. bijuga* colony as depicted in Fig. 2 of Ref. [23]. The simulated axisymmetric colony consists of seven laterally distributed jets that are prescribed with the observed jet angles, i.e., 68.4°, 57.2°, 52.8°, 49.8°, 48.9°, 45.3°, and 44.7°, starting from the one closest to the anterior of the colony. Plotted here are the simulated jet velocity U_{jet} (a), drag coefficient C_D (b), quasipropulsive efficiency η_{QPE} (c), and Froude propulsion efficiency η_{FPE} (d) as functions of Re. Simulated C_D's for a steadily towed axisymmetric body of the same body length are also plotted in (b).

disappear around the head region and the flow fields are also narrower around the body; the velocity magnitude field of L4 [Fig. 7(c)] decays spatially faster than those of R4 [Fig. 7(g)] and T4 [Fig. 7(k)] but only behind the body and only slightly slower laterally to the body. In contrast to $\text{Re} = 18.9$, the pressure field of R4 has a negative pressure zone with weak pressure gradients associated with its rear jet [Fig. 7(h)].

These CFD simulation results demonstrate that at intermediate Re's the flow field imposed by a self-propelled, steadily swimming body is completely different from that of a body that is towed at the same speed and that the differences are both propulsion strategy dependent and Re dependent.

B. Optimal jet angles

A body, which swims by issuing laterally distributed multijets at the same jet angle, maximizes its quasipropulsive efficiency η_{QPE} at an optimal jet angle that depends only weakly on Re [Fig. 8(a)], and it maximizes its Froude propulsion efficiency η_{FPE} at a different optimal jet angle that decreases slightly as Re increases [Fig. 8(b)].

The existence of these two types of optimal jet angles is rooted in the patterns by which the drag coefficient C_D, the useful power P_{useful}, and the jet power P_{jet} vary with the jet angle θ [Figs. 8(c), 8(e), and 8(f)]. For a given Re, C_D decreases as θ increases [Fig. 8(c)] because the interaction between the multijets and the lateral boundary-layer flow of the body decreases as θ increases.

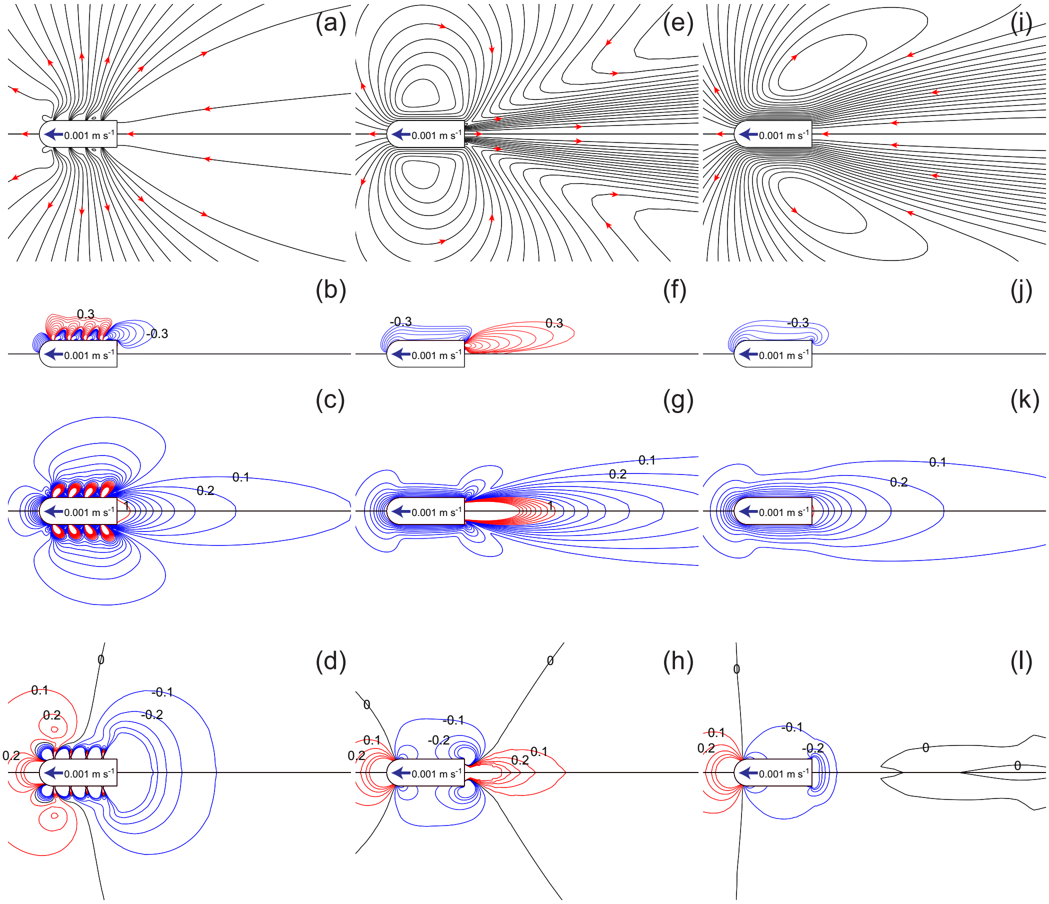

FIG. 6. Re = 18.9. CFD simulated flow fields imposed by an L4 body that adopts the same jet angle of 70° for all four lateral jets and swims at 0.001 m/s [(a)–(d)], an R4 body that swims at 0.001 m/s using a rear jet [(e)–(h)], and a T4 body that is towed at 0.001 m/s [(i)–(l)]. (a), (e), (i) Streamline patterns in a stationary frame of reference. (b), (f), (j) Contours of azimuthal vorticity scaled by U/R; red contour levels are 0.300, 0.443, 0.654, 0.965, 1.420, 2.100, 3.110, 4.590, 6.770, and 10.000; blue contour levels are −0.300, −0.443, −0.654, −0.965, −1.420, −2.100, −3.110, −4.590, −6.770, and −10.000. (c), (g), (k) Contours of velocity magnitude in a stationary frame of reference and scaled by U; red contour levels start from 1.0 with increment 0.1; blue contour levels start from 0.1 to 0.9 with increment 0.1. (d), (h), (l) Contours of pressure scaled by $0.5\rho U^2$; red contour levels start from 0.1 with increment 0.1; blue contour levels start from −0.1 with increment −0.1; black contour lines are 0.

Consequently, P_{useful} decreases as θ increases [Fig. 8(e)]. The jet power P_{jet}, however, becomes higher when θ approaches either 0° or 90° [Fig. 8(f)] because for the former more jet power is needed to overcome the increased drag while for the latter more jet power is needed to compensate the increased jet angle. The tow power P_{tow}, of course, does not vary with θ [Fig. 8(d)]. Thus, the calculation combining P_{tow} and P_{jet} based on Eq. (10) leads to the prediction of an optimal jet angle that maximizes η_{QPE} [Fig. 8(a)], while the calculation combining P_{uesful} and P_{jet} based on Eq. (8) leads to the prediction of another optimal jet angle that maximizes η_{FPE} [Fig. 8(b)], for a given Re.

The results for all L1–L7 bodies follow the similar patterns as above described, and a summary of the results is presented in Fig. 9. The optimal jet angle θ_{maxQPE}, which maximizes the quasipropulsive efficiency for a given Re, ranges from 70° to 61° for a range of Re × e from 6.5 to 650.4

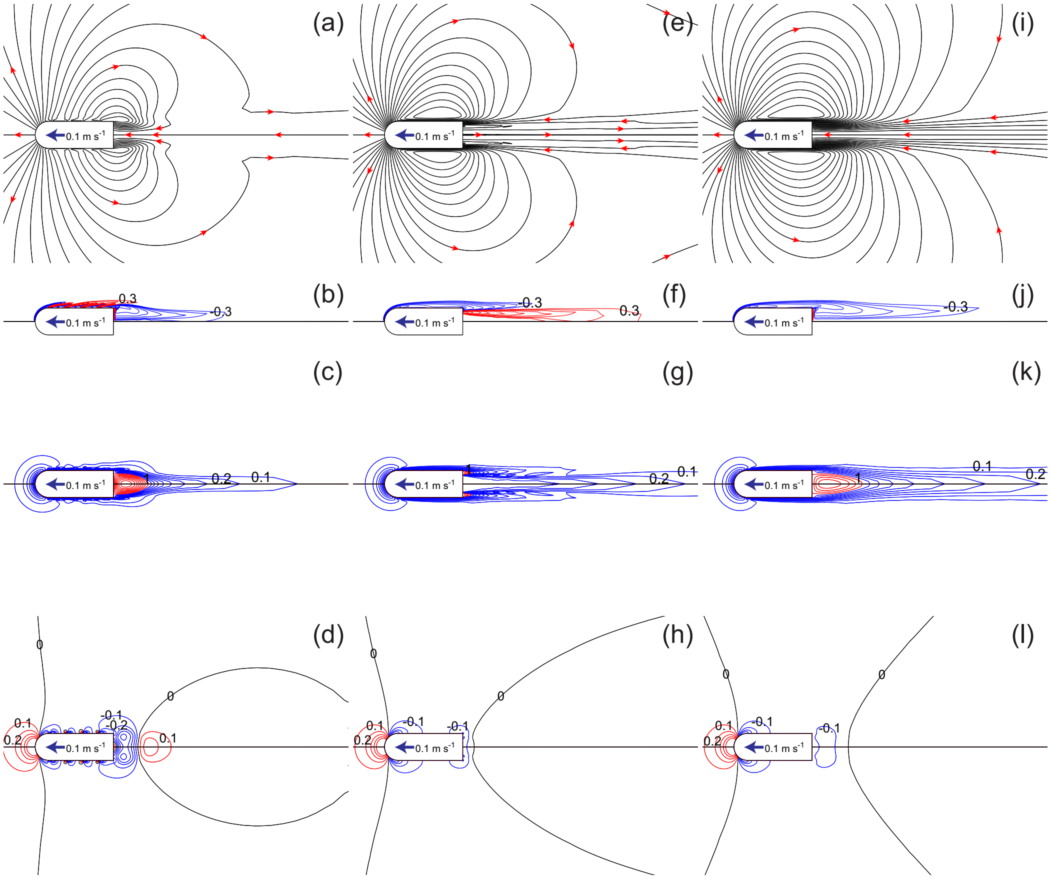

FIG. 7. Re = 1886.1. CFD-simulated flow fields imposed by an L4 body that adopts the same jet angle of 64° for all four lateral jets and swims at 0.1 m/s [(a)–(d)], an R4 body that swims at 0.1 m/s using a rear jet [(e)–(h)], and a T4 body that is towed at 0.1 m/s [(i)–(l)]. (a), (e), (i) Streamline patterns in a stationary frame of reference. (b), (f), (j) Contours of azimuthal vorticity scaled by U/R; red contour levels are 0.300, 0.443, 0.654, 0.965, 1.420, 2.100, 3.110, 4.590, 6.770, and 10.000; blue contour levels are −0.300, −0.443, −0.654, −0.965, −1.420, −2.100, −3.110, −4.590, −6.770, and −10.000. (c), (g), (k) Contours of velocity magnitude in a stationary frame of reference and scaled by U; red contour levels start from 1.0 with increment 0.1; blue contour levels start from 0.1 to 0.9 with increment 0.1. (d), (h), (l) Contours of pressure scaled by $0.5\rho U^2$; red contour levels start from 0.1 with increment 0.1; blue contour levels start from −0.1 with increment −0.1; black contour lines are 0.

[Fig. 9(a)], equivalent to swimming speeds ranging from 0.001 to 0.1 m/s. The optimal jet angle θ_{maxFPE}, which maximizes the Froude propulsion efficiency for a given Re, decreases from 45° to 34° as Re × e increases from 6.5 to 650.4 [Fig. 9(e)]. The achieved maximum quasipropulsive efficiency $\eta_{\mathrm{QPE,max}}$ increases as Re × e increases for a given body configuration, but decreases as the number of jet modules increases from 1 in L1 to 7 in L7 for a given Re × e [Fig. 9(b)]. In contrast, the achieved maximum Froude propulsion efficiency $\eta_{\mathrm{FPE,max}}$ increases both as Re × e increases for a given body configuration and as the number of jet modules increases from 1 in L1 to 7 in L7 for a given Re × e [Fig. 9(f)]. These two different variation patterns are closely related to the patterns by which the tow power P_{tow}, the $\eta_{\mathrm{QPE,max}}$-associated jet power $P_{\mathrm{jet,maxQPE}}$, the $\eta_{\mathrm{FPE,max}}$-associated useful power $P_{\mathrm{useful,maxFPE}}$, and the $\eta_{\mathrm{FPE,max}}$-associated jet power $P_{\mathrm{jet,maxFPE}}$ vary with Re × e [Figs. 9(c), 9(d), 9(g), and 9(h)].

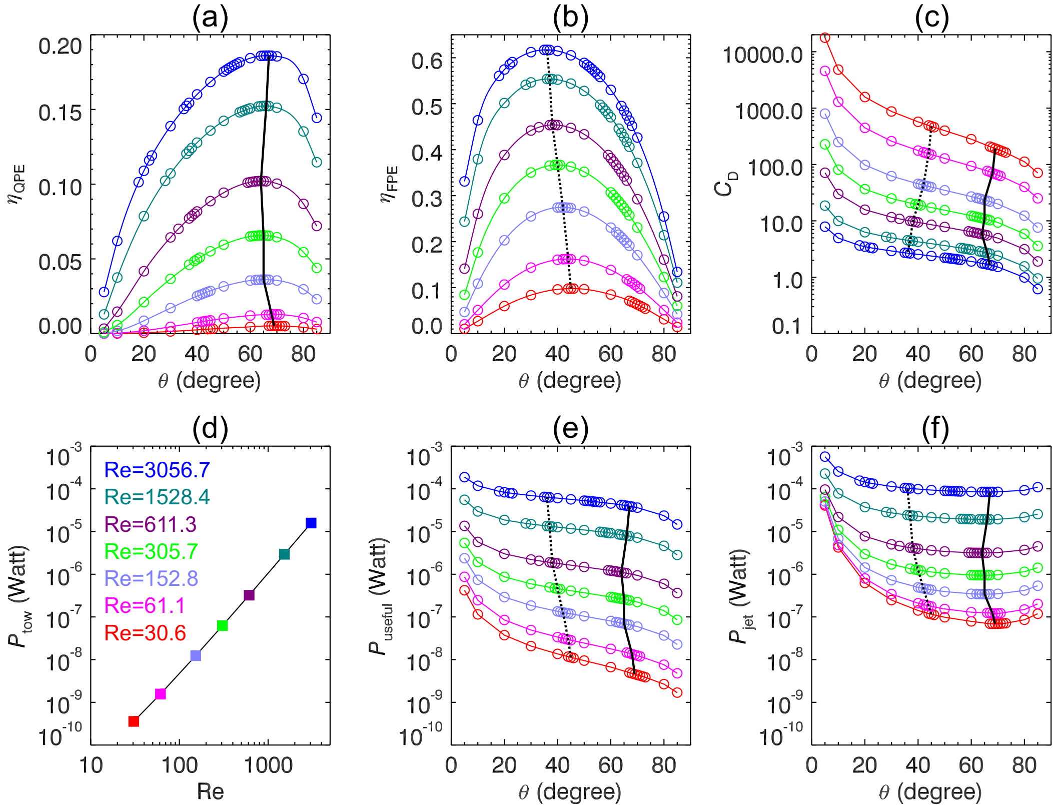

FIG. 8. An L7 body swims by adopting the same jet angle for all its seven lateral jets. The jet angle varies between 5° and 85° for each of the considered seven Re's (color coded). Line plots of (a) the quasipropulsive efficiency η_{QPE}, (b) the Froude propulsion efficiency η_{FPE}, (c) the drag coefficient C_D, (e) the useful power P_{useful}, and (f) the jet power P_{jet} against the jet angle θ. (d) Line plot of the tow power P_{tow} against Re. In (a), (c), (e), or (f), the solid black line shows the optimal jet angles that maximize η_{QPE}. In (b), (c), (e), or (f), the dotted black line shows the optimal jet angles that maximize η_{FPE}.

Reference [23] reported that a video-recorded swimming of an *N. bijuga* colony adopted jet angles of 68.4°, 57.2°, 52.8°, 49.8°, 48.9°, 45.3°, and 44.7°, respectively, for its jet modules starting from the one closest to the anterior of its nectosome. Those jet angles observed for the jet modules that were near the anterior of the nectosome fall approximately in the CFD-predicted range of the optimal jet angle θ_{maxQPE} that maximizes the quasipropulsive efficiency η_{QPE} for a given Re. Those observed jet angles close to the rear part of the nectosome conform to the upper bound of the CFD-predicted range of the optimal jet angle θ_{maxFPE} that maximizes the Froude propulsion efficiency η_{FPE} for a given Re. The CFD simulations of the colonial swimming that adopts the observed jet angles show that both η_{QPE} and η_{FPE} are, respectively, smaller (only slightly) than those under the two types of optimal jet angles [Fig. 5(c) vs L7 of Fig. 9(b); Fig. 5(d) vs L7 of Fig. 9(f)]. Thus, the real colony adopts a spatial pattern of jet angles that may be a compromise or tradeoff between the two types of optimal jet angles (i.e., θ_{maxQPE} that maximizes η_{QPE}, thereby minimizing the mechanical power consumption for propulsion; θ_{maxFPE} that maximizes η_{FPE}, thereby minimizing the wake). Specifically, anterior nectophores are usually smaller because they are more recently developed. These small individuals produce jets of similar angles to the η_{QPE} optimum that allows maximum power efficiency. In contrast, posterior nectophores have much lower jet angles resembling the η_{FPE} optimum that minimize wake disturbance and potential damage to the colony

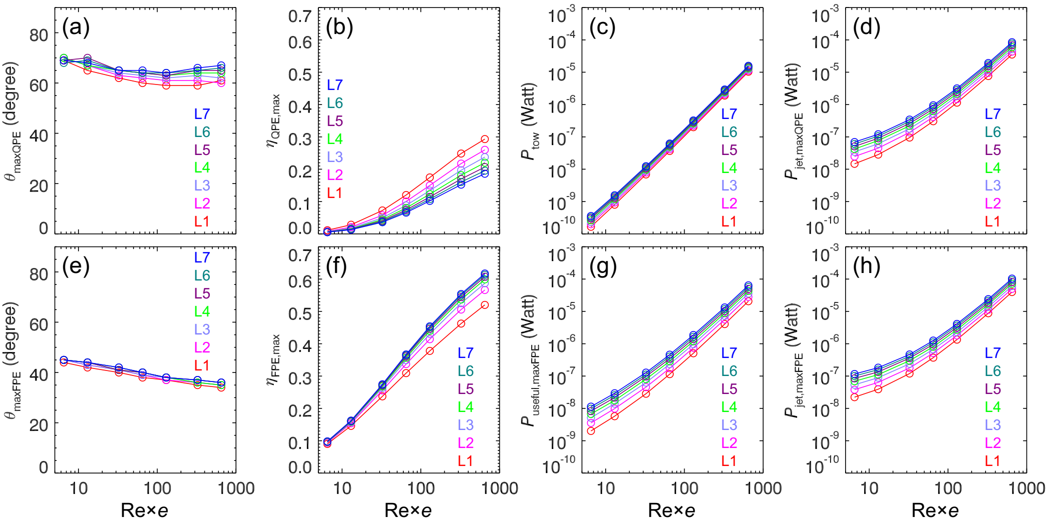

FIG. 9. Line plots of (a) the optimal jet angle θ_{maxQPE}, (b) the achieved maximum quasipropulsive efficiency $\eta_{\mathrm{QPE,max}}$, (c) the tow power P_{tow}, and (d) the $\eta_{\mathrm{QPE,max}}$-associated jet power $P_{\mathrm{jet,maxQPE}}$ against Re × e. Line plots of (e) the optimal jet angle θ_{maxFPE}, (f) the achieved maximum Froude propulsion efficiency $\eta_{\mathrm{FPE,max}}$, (g) the $\eta_{\mathrm{FPE,max}}$-associated useful power $P_{\mathrm{useful,maxFPE}}$, and the $\eta_{\mathrm{FPE,max}}$-associated jet power $P_{\mathrm{jet,maxFPE}}$ against Re × e. The lines are color coded by the L1–L7 bodies.

members of the siphosome. The jet angle varies systematically along the length of the nectosome, so the primary contributions of nectophores to propulsion depend upon their position in the nectosome with the anteriormost determining primarily rotation while the remainder contribute primarily to translation [23]. Nevertheless, more observational data of the jet angles are still needed, and CFD simulations that consider additional biological complexity, e.g., different speeds and/or jet angles for different jet modules, are also needed, in order ultimately to inform the mechanisms of the optimal jet angles.

C. Energetic benefits for colonial swimming via laterally distributed multijets

Under the condition of achieving the maximum quasipropulsive efficiency as above described, the mechanical power per jet module $P_{\text{jet-module}}$ is calculated as P_{mj}/N, where P_{mj} is the total jet power [Eq. (5)] and N is the number of jet modules in the swimming body, and the results are presented in Fig. 10(a). For a given body configuration (i.e., each of the L1–L7 bodies), $P_{\text{jet-module}}$ increases as the swimming speed U increases. For a given U (i.e., each of the considered swimming speeds from 0.001 to 0.1 m/s), $P_{\text{jet-module}}$ decreases as the number of jet modules increases from 1 in L1 to 7 in L7.

Next, the mechanical power P_{solitary} required for the lone jet module in the L1 body to swim at a given U is used to normalize $P_{\text{jet-module}}$ calculated for each of the L1–L7 bodies swimming at the same speed U [Fig. 10(b)]. The results of $P_{\text{jet-module}}/P_{\mathrm{solitary}} \times 100$ show that significant energetic benefits are achieved for individual jet modules to swim within a colony compared with solitarily swimming. The higher the number of jet modules of the colony, the higher the energetic benefit for each participating jet module. Also, the faster the swimming speed of the colony, the higher is the energetic benefit for each participating jet module. For example, each jet module in the L7 body that swims at 0.001 m/s spends ∼67% of the power that the lone jet module in the L1 body spends to swim at the same speed; when all are swimming at 0.1 m/s, each jet module in the L7 body spends only ∼34% of the power that the lone jet module in the L1 body expends, while each jet module in the L4 body spends ∼42% of the power that the lone jet module in the L1 body expends.

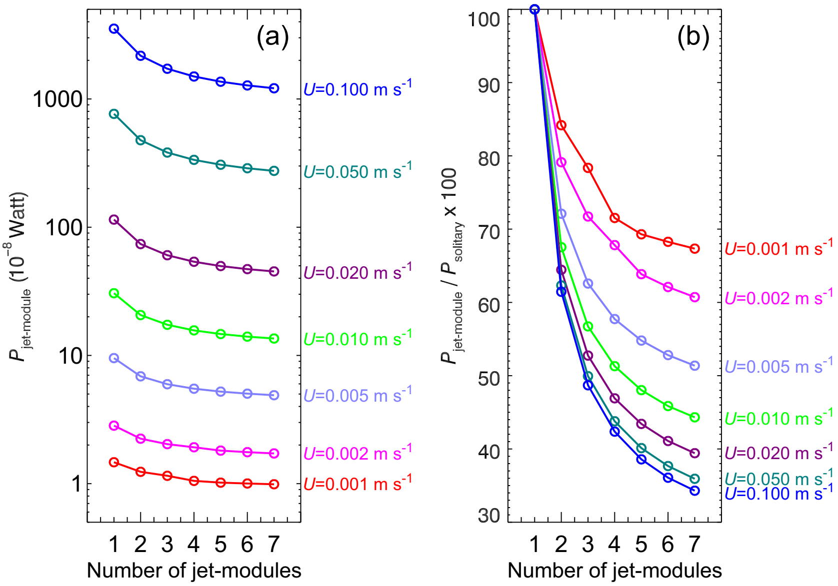

FIG. 10. Line plots of (a) $P_{\text{jet-module}}$ and (b) $P_{\text{jet-module}}/P_{\text{solitary}} \times 100$ against the number of jet modules in the swimming body that is propelled by laterally distributed multijets. The lines are color coded by the swimming speed U. See the main text for details of the variables.

D. Comparing laterally distributed multijet propulsion with rear-jetting single-jet propulsion

The L1–L7 bodies that swim via the laterally distributed multijet propulsion reach much lower quasipropulsive efficiencies than those attained by the R1–R7 bodies that swim via the rear-jetting single-jet propulsion [Fig. 11(a) vs Fig. 11(c)]. This is consistent with the results that the former requires much higher total jet powers than the latter [Fig. 9(d) vs Fig. 11(d)]. Thus, at the whole-colony level, the laterally distributed multijet propulsion is energetically less efficient than the rear-jetting single-jet propulsion in the considered $\mathrm{Re} \times e$ range of 5–1000.

In contrast, at the level of individual jet modules that participate in colonial swimming, the power cost for each participating jet module is comparable to or even lower than the jet power that is required by the rear-jetting single-jet propulsion to swim at the same $\mathrm{Re} \times e$ [Fig. 11(b) vs Fig. 11(d)]. For example, a solitary jet module (i.e., the L1 body) spends 3.53×10^{-5} W in order to swim at 0.1 m/s. If it participates in a colony consisting of seven jet modules (i.e., the L7 body), the same jet module spends only 1.21×10^{-5} W in order to swim at 0.1 m/s as a part of colonial swimming. This power is even less than the jet power of 2.54×10^{-5} W that the R7 body spends in order to swim at 0.1 m/s. Thus, the laterally distributed multijet propulsion provides a viable way for individual nectophores (i.e., the energy-limited jet modules) to achieve high swimming speeds by being a part of colonial swimming, thereby reducing the jet power each individually.

How a swimming body propels itself through water impacts the drag force it experiences (Fig. 12). The L1–L7 bodies that swim via the laterally distributed multijet propulsion experiences lower pressure drag coefficients $C_{D\text{-pressure}}$ but significantly higher viscous drag coefficients $C_{D\text{-viscous}}$ than those experienced by the R1–R7 bodies that swim via the rear-jetting single-jet propulsion [Fig. 12(b) vs Fig. 12(f); Fig. 12(c) vs Fig. 12(g)]. As a result, the former experiences significantly higher overall drag coefficients C_D than those experienced by the latter [Fig. 12(a) vs Fig. 12(e)]. In the laterally distributed multijet propulsion [Fig. 13(a)], because of the interaction between the lateral jets and the laminar boundary-layer flow along the lateral surface of the swimming body, the wall shear in the lateral boundary layer is much stronger than in the rear-jetting single-jet propulsion

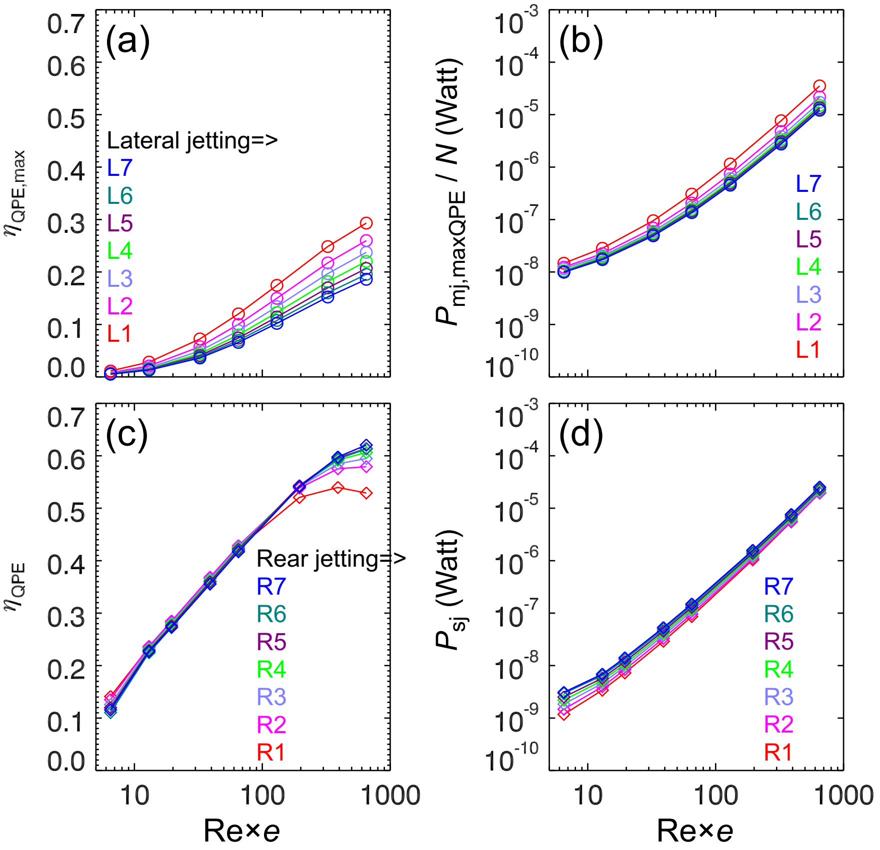

FIG. 11. Line plots of (a) the achieved maximum quasipropulsive efficiency $\eta_{\mathrm{QPE,max}}$ and (b) the $\eta_{\mathrm{QPE,max}}$-associated mechanical power per jet module $P_{\mathrm{mj,maxQPE}}/N$ against Re × e, for the L1–L7 bodies (color coded) that swim via the laterally distributed multijet propulsion. Line plots of (c) the quasipropulsive efficiency η_{QPE} and (d) the jet power P_{sj} against Re × e, for the R1–R7 bodies (color coded) that swim via the rear-jetting single-jet propulsion.

[Fig. 13(b)] and in the towed body case [Fig. 13(c)]. This is the reason for the significantly higher $C_{D\text{-viscous}}$ in the laterally distributed multijet propulsion.

For a swimming colony that consists of multiple jet modules (e.g., $\geqslant 5$), its drag force is due predominantly to viscous drag [Fig. 12(d)] that is to some degree proportional to the lateral surface area of the colony; however, its thrust is proportional to the number of jet modules and therefore scaled with the colony-body volume. As the number of jet modules increases, the supply of thrust exceeds the increasing drag force, thereby affording an even higher swimming speed. This crude scaling argument indicates that the laterally distributed multijet propulsion is a highly feasible way for the energy-limited cnidarian swimmers to attain high swimming speeds via colonial swimming. Unlike animal groups such as squid or chordates, the ability of cnidarians to generate muscular force is constrained by the evolutionary limits of their muscle design. Whereas other animal phyla possess true muscles, cnidarians possess only muscular fibers that are contained within a single layer of epithelial cells. This configuration limits muscular force generation and affects the volume of fluid that individual nectophores can accelerate as a high-velocity jet [49]. Consequently, energy efficiency is an important component of nectophore design. Although the total length of siphonophore nectosomes may be tens of centimeters, individual nectophores are of

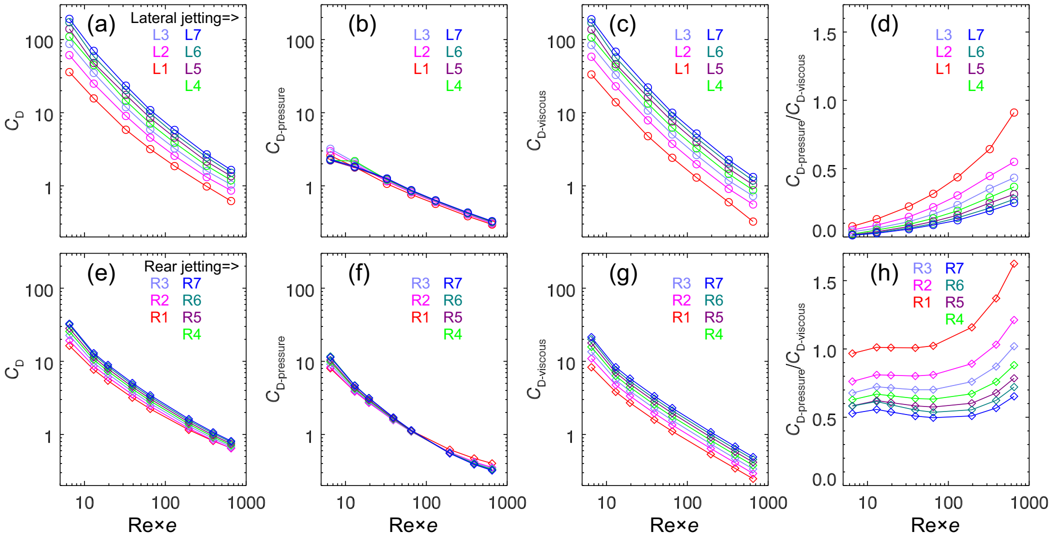

FIG. 12. Line plots of (a) C_D, (b) $C_{D\text{-pressure}}$, (c) $C_{D\text{-viscous}}$, and (d) $C_{D\text{-pressure}}/C_{D\text{-viscous}}$ against Re × e, for the L1–L7 bodies (color coded) that swim via the laterally distributed multijet propulsion. Line plots of (e) C_D, (f) $C_{D\text{-pressure}}$, (g) $C_{D\text{-viscous}}$, and (h) $C_{D\text{-pressure}}/C_{D\text{-viscous}}$ against Re × e, for the R1–R7 bodies (color coded) that swim via the rear-jetting single-jet propulsion.

small sizes that permit efficient jet production by their limited muscular arrays [50]. On the other hand, despite its high quasipropulsive efficiency, the rear-jetting single-jet propulsion demands the generation of high thrust by a single jet in order to swim rapidly. Thus, only the squidlike animals that have strong and massive muscle mass can afford this propulsion mode at high swimming speeds.

The primary function of the nectosome is to pull the siphosome through water. It is thus beneficial if the flow imposed by the propulsive nectosome inflicts a minimal impact on the siphosome that is made up of the feeding and reproductive members of the colony. Compared with the rear-jetting single-jet propulsion, the laterally distributed multijet propulsion has a much weaker flow field [Fig. 14(a) vs Fig. 14(b)] and a weaker and spatially more limited rate of deformation field in the wake region [Fig. 15(a) vs Fig. 15(b)]. Thus, the present CFD simulations describe a multijet system that allows the nectosome to transport the colony with minimal damage to the siphosome. In contrast, a squidlike rear-jetting single-jet propulsion would tow the siphosome but the strong backward jet would directly impact the siphosome, thereby inducing additional drag and damaging colony members comprising the siphosome.

Figure 16 shows flow velocity vector fields in a stationary frame of reference, to further illustrate the different flow patterns between these two jet-propulsion strategies and, in particular, the alteration by the laterally distributed multijets to the lateral boundary-layer flow along the swimming body.

IV. CONCLUSION

A CFD approach has been developed to simulate the flow fields imposed by a self-propelled axisymmetric body that swims steadily via the laterally distributed multijet propulsion at intermediate Reynolds numbers on the orders of 1–1000. The aim is to shed light on the fluid mechanics and adaptive values of the multijet propelled colonial swimming in physonect siphonophores. For comparative purposes, the flow fields have also been simulated for a self-propelled body that swims via the rear-jetting single-jet propulsion and for a towed body. The simulation results show that

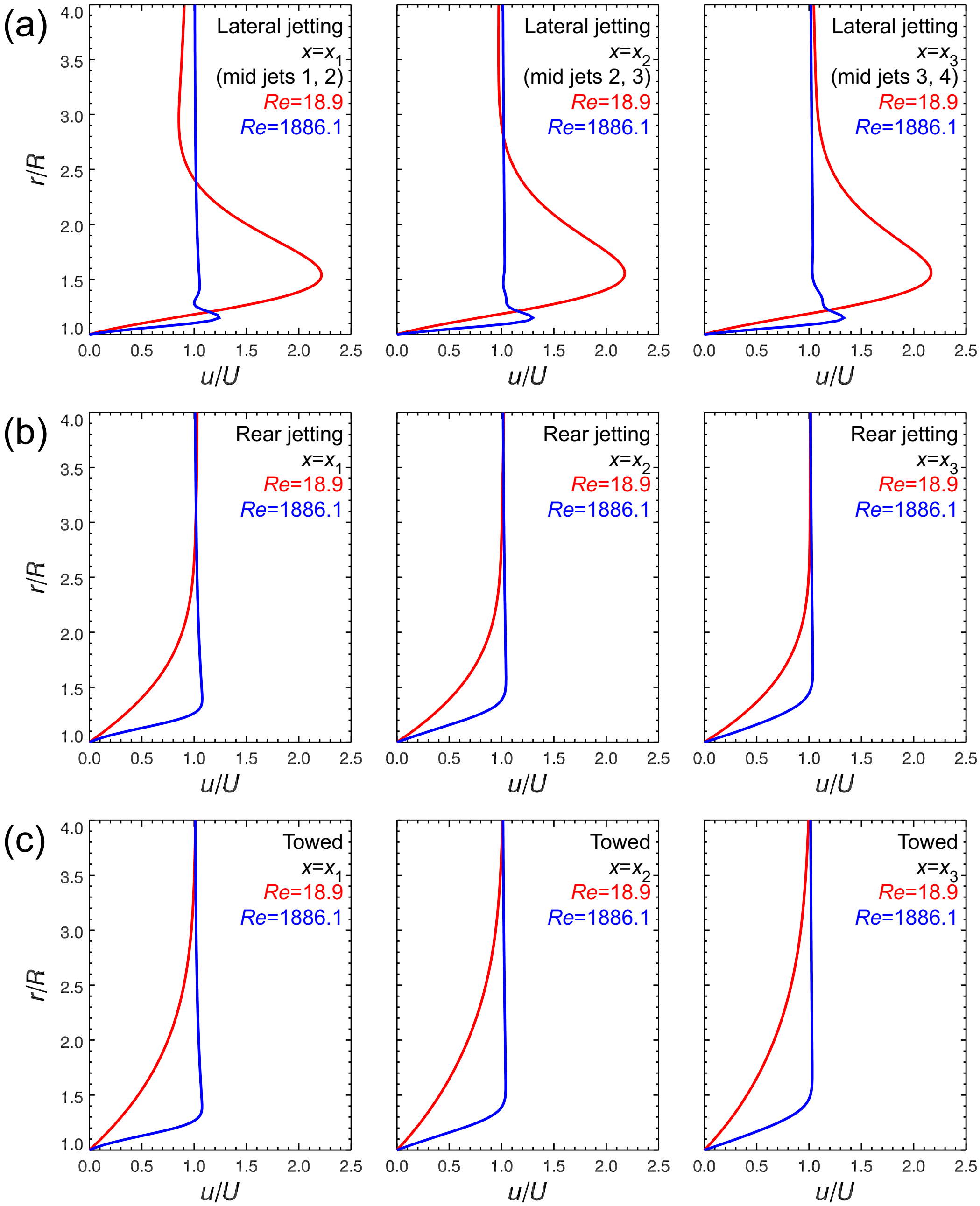

FIG. 13. Lateral boundary-layer velocity profiles, u/U against r/R, plotted for (a) the L4 body that swims via the laterally distributed multijet propulsion at the maximum quasipropulsive efficiency, (b) the R4 body that swims via the rear-jetting single-jet propulsion, and (c) the T4 body that is towed through water, respectively, at two Re values (color coded).

the imposed flow fields, drag coefficients, mechanical powers, and swimming efficiencies all vary significantly with different propulsion strategies and Reynolds numbers, and with different jet angles in the laterally distributed multijet propulsion.

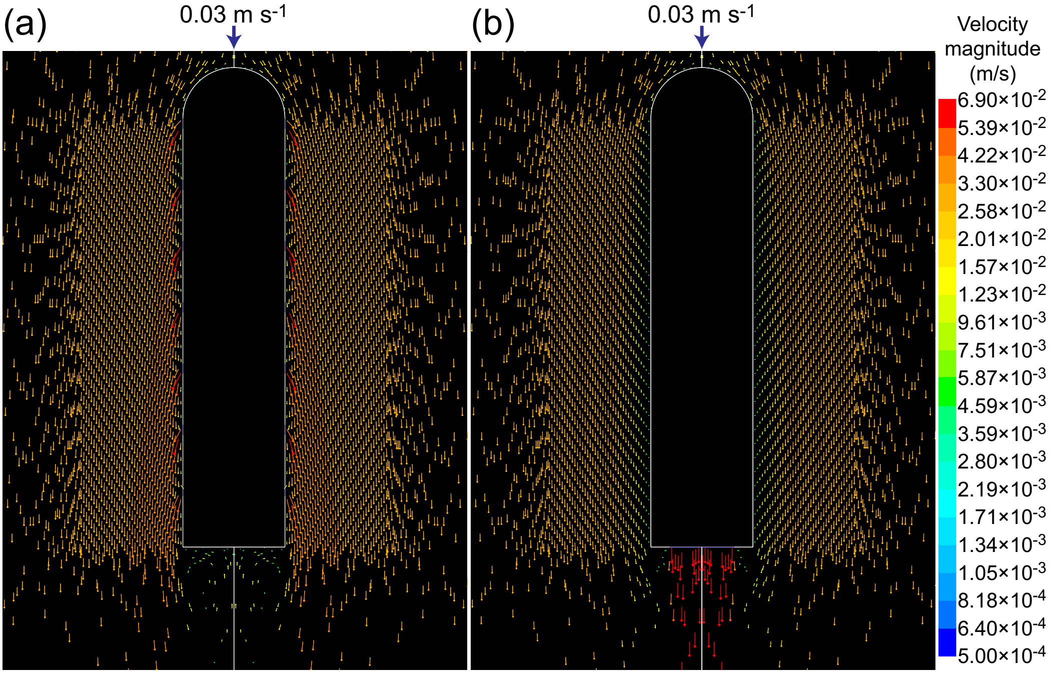

FIG. 14. Re = 917.0. Flow velocity vector fields (in a frame of reference fixed on the body) for (a) the L7 body that swims at 0.03 m/s via seven laterally distributed jets that are prescribed with the observed jet angles, i.e., 68.4°, 57.2°, 52.8°, 49.8°, 48.9°, 45.3°, and 44.7°, starting from the one closest to the anterior of the colony (as in a video-recorded swimming of an *N. bijuga* colony as depicted in Fig. 2 of Ref. [23]), and (b) the R7 body that swims at 0.03 m/s via the rear-jetting single-jet propulsion. For clarity, only 4.5% of total vectors are shown.

For the laterally distributed multijet propulsion, two types of optimal jet angles have been determined from simulations where all lateral jets in each case adopt the same jet angle. For a given Reynolds number, the optimal jet angle that maximizes the quasipropulsive efficiency ranges from 70° to 61°, while the optimal jet angle that maximizes the Froude propulsion efficiency ranges from 45° to 34°. A real swimming physonect siphonophore has jet angles for anteriormost several jet modules that match the predicted range maximizing the quasipropulsive efficiency (thereby minimizing the jet power). Posterior nectophores adopt jet angles that resemble more closely the upper bound of the optimal jet angles maximizing the Froude propulsion efficiency (thereby minimizing the wake). Therefore, nectophores of actual siphonophores may shift function as they develop from newly budded, small individuals as the anterior of the nectosome to older, mature individuals as the posterior of the nectosome. This model indicates the relative advantages of the different stages in this developmental sequence.

Individual jet modules belonging to a colony that swims at a given speed require a significantly lower per-module power than that required by a lone jet module that swims solitarily at the same speed; the higher the number of jet modules of the colony, the lower the per-module power consumption by each participating jet module of the colony.

Because of the interaction between its lateral jets and the laminar boundary-layer flow along its lateral surface, a body that swims via the laterally distributed multijet propulsion experiences a significantly higher viscous drag and therefore a significantly higher overall drag coefficient than if it swims via the rear-jetting single-jet propulsion. As a result, the laterally distributed multijet propulsion is energetically less efficient than the rear-jetting single-jet propulsion. Nevertheless,

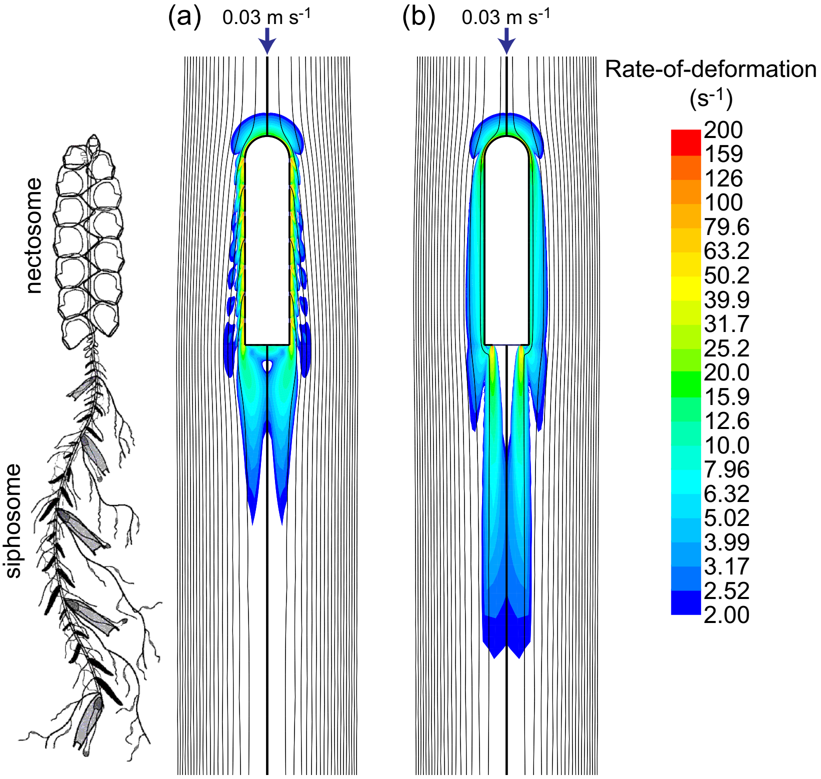

FIG. 15. Re = 917.0. Filled color contours of the rate of deformation field overlapping with black streamlines (in a frame of reference fixed on the body) for the same two cases as in Fig. 14.

the per-module power consumption by each participating jet module of the colonial swimming is comparable to or even lower than the single-jet power that is required by the rear-jetting single-jet propulsion to swim at the same Reynolds number.

For a colony that swims via the laterally distributed multijet propulsion, the drag force is more or less proportional to the lateral surface area of the colony, while the thrust is proportional to the number of jet modules and therefore scaled with the colony-body volume. With increasing the number of jet modules, the supply of thrust can always surpass the increasing drag force. Thus, the laterally distributed multijet propulsion is a highly feasible way for the energy-limited cnidarian swimmers to attain high swimming speeds via colonial swimming.

In the multijet propelled colonial swimming of a physonect siphonophore, the nectosome functions to transport the entire colony (nectosome and trailing siphosome). In contrast to propulsion using a rear-jetting single jet, the laterally distributed multijets characterizing the siphonophore nectosome successfully transport the colony while minimizing disturbance to the colony members in the trailing siphosome.

The present study assumes steady axisymmetric flow, which is a compromise between the complex biological reality and the numerical tractability as well as computational efficiency to simulate the problem. To explore the parameter space, this study has conducted 1280 simulations, which has been made possible by the steady axisymmetric flow assumption. If unsteady flow with full three-dimensional (3D) realistic geometry were considered, the required computational resources would be very high. The steady axisymmetric flow assumption is suitable because it captures two essential characteristics of laterally distributed multijet propulsion, namely (1) multiple lateral jets are being issued into a lateral boundary-layer flow; and (2) the total length of the swimming body

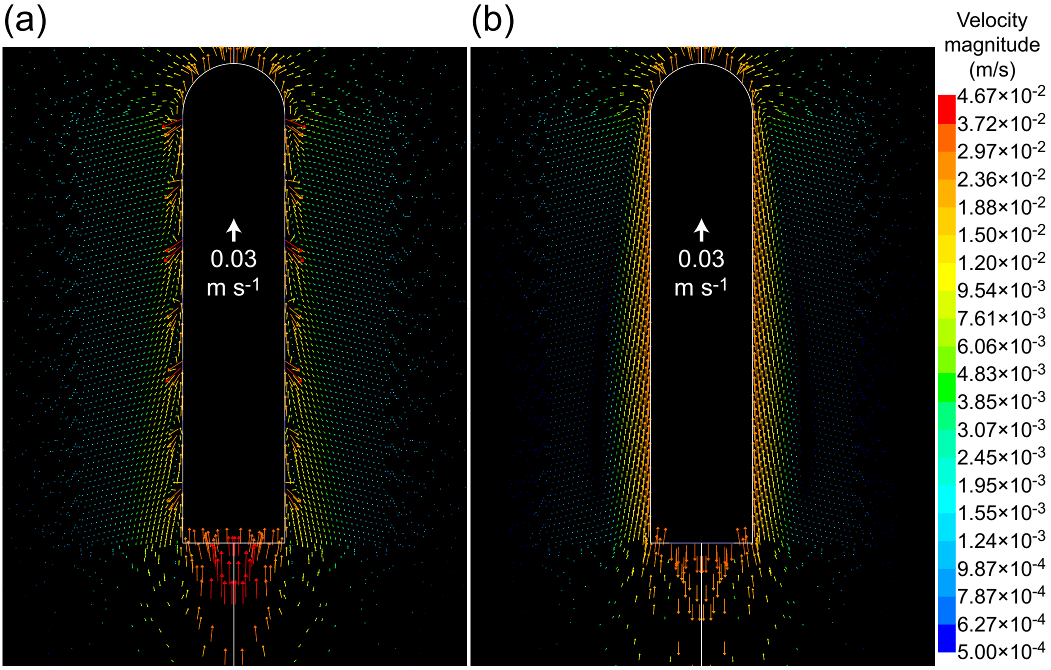

FIG. 16. Re = 917.0. Flow velocity vector fields (in a stationary frame of reference) for the same two cases as in Fig. 14. For clarity, only 5.2% of total vectors are shown.

is linearly proportional to the total number of jets. As described above, the simulation results seem to be consistent with currently available biological observations, and are useful for understanding some of the fundamental mechanisms of colonial swimming via laterally distributed multijet propulsion in physonect siphonophores. Nevertheless, unsteady full 3D flow models are required to tackle problems with additional biological and hydrodynamic complexities. For example, the lateral jets issued by individual nectophores have leading vortex rings; how does vortex dynamics affect the propulsion performance, with comparison with jellyfish jet propulsion with vortex rings [37,38,41,49]? Colonial physonect siphonophores can cruise at rather constant speeds, accelerate quickly, or turn agilely [23,25]. How the lateral jets fire synchronously or asynchronously at suitable angles and speeds to achieve these remains an important question to investigate numerically. A theoretical hydrodynamic analysis has suggested that asynchronous firing is advantageous for maintaining a more constant speed in salp chains [28]. Additionally, the jet-firing and fluid-refilling cycle may potentially provide a mechanism to control the lateral boundary-layer flow along the nectosome surface (Video 3 of Supplemental Material [21]). It has been suggested that refilling leads to a high-pressure region that generates forward thrust, thereby enhancing overall swimming performance [24]. A more traditional idea may suggest that suction associated with fluid refilling of nectophores reduces the thickness of the boundary layer by removing the fluid next to the nectosome surface, thereby resulting in a more stable layer and delayed transition to turbulence (Fig. 8 of Ref. [33]). These are interesting questions that may require unsteady full 3D flow simulations.

ACKNOWLEDGMENTS

This work was supported by a Woods Hole Oceanographic Institution (WHOI) Independent Research and Development (IR&D) fund to H.J. The authors also acknowledge the support of National Science Foundation Grants No. OCE-1559062 and No. IOS-1353937 to H.J., No. OCE-1830015 to

J.H.C., and No. OCE-1829913 to S.P.C. The authors thank two anonymous reviewers for providing helpful and constructive comments that improved the manuscript.

---

[1] S. Vogel, *Life in Moving Fluids: The Physical Biology of Flow* (Princeton University Press, Princeton, NJ, 1994).

[2] Q. Bone and E. R. Trueman, Jet propulsion in salps (Tunicata: Thaliacea), J. Zool. Lond. **201**, 481 (1983).

[3] L. P. Madin, Aspects of jet propulsion in salps, Can. J. Zool. **68**, 765 (1990).

[4] K. R. Sutherland and L. P. Madin, Comparative jet wake structure and swimming performance of salps, J. Exp. Biol. **213**, 2967 (2010).

[5] T. L. Daniel, Mechanics and energetics of medusan jet propulsion, Can. J. Zool. **61**, 1406 (1983).

[6] S. P. Colin and J. H. Costello, Morphology, swimming performance and propulsive mode of six co-occurring hydromedusae, J. Exp. Biol. **205**, 427 (2002).

[7] J. O. Dabiri, S. P. Colin, J. H. Costello, and M. Gharib, Flow patterns generated by oblate medusan jellyfish: Field measurements and laboratory analyses, J. Exp. Biol. **208**, 1257 (2005).

[8] K. Katija and H. Jiang, Swimming by medusae *Sarsia tubulosa* in the viscous vortex ring limit, Limnol. Oceanogr. Fluids Environ. **3**, 103 (2013).

[9] K. Katija, S. P. Colin, J. H. Costello, and H. Jiang, Ontogenetic propulsive transitions by *Sarsia tubulosa* medusae, J. Exp. Biol. **218**, 2333 (2015).

[10] R. L. Marsh, J. M. Olson, and S. K. Guzik, Mechanical performance of scallop adductor muscle during swimming, Nature (London) **357**, 411 (1992).

[11] J.-Y. Cheng and M. E. DeMont, Jet-propelled swimming in scallops: Swimming mechanics and ontogenic scaling, Can. J. Zool. **74**, 1734 (1996).

[12] A. Packard, Q. Bone, and M. Hignette, Breathing and swimming movements in a captive nautilus, J. Mar. Biol. Assoc. UK **60**, 313 (1980).

[13] R. K. O'Dor, J. Wells, and M. J. Wells, Speed, jet pressure and oxygen consumption relationships in free-swimming *Nautilus*, J. Exp. Biol. **154**, 383 (1990).

[14] T. R. Neil and G. N. Askew, Swimming mechanics and propulsive efficiency in the chambered nautilus, R. Soc. Open Sci. **5**, 170467 (2018).

[15] W. Johnson, P. D. Soden, and E. R. Trueman, A study in jet propulsion: An analysis of the motion of the squid, *Loligo vulgaris*, J. Exp. Biol. **56**, 155 (1972).

[16] R. K. O'Dor, The forces acting on swimming squid, J. Exp. Biol. **137**, 421 (1988).

[17] R. K. O'Dor and D. M. Webber, Invertebrate athletes: Trade-offs between transport efficiency and power density in cephalopod evolution, J. Exp. Biol. **160**, 93 (1991).

[18] E. J. Anderson and M. E. DeMont, The mechanics of locomotion in the squid *Loligo pealei*: Locomotory function and unsteady hydrodynamics of the jet and intramantle pressure, J. Exp. Biol. **203**, 2851 (2000).

[19] E. J. Anderson and M. A. Grosenbaugh, Jet flow in steadily swimming adult squid, J. Exp. Biol. **208**, 1125 (2005).

[20] I. K. Bartol, P. S. Krueger, W. J. Stewart, and J. T. Thompson, Hydrodynamics of pulsed jetting in juvenile and adult brief squid *Lolliguncula brevis*: Evidence of multiple jet 'modes' and their implications for propulsive efficiency, J. Exp. Biol. **212**, 1889 (2009).

[21] See Supplemental Material at http://link.aps.org/supplemental/10.1103/PhysRevFluids.6.013103 for three videos of animal jet propulsion.

[22] G. O. Mackie, Analysis of locomotion in a siphonophore colony, Proc. R. Soc. B **159**, 366 (1964).

[23] J. H. Costello, S. P. Colin, B. J. Gemmell, J. O. Dabiri, and K. R. Sutherland, Multi-jet propulsion organized by clonal development in a colonial siphonophore, Nat. Commun. **6**, 8158 (2015).

[24] K. R. Sutherland, B. J. Gemmell, S. P. Colin, and J. H. Costello, Propulsive design principles in a multi-jet siphonophore, J. Exp. Biol. **222**, jeb198242 (2019).

[25] K. R. Sutherland, B. J. Gemmell, S. P. Colin, and J. H. Costello, Maneuvering performance in the colonial siphonophore, *Nanomia bijuga*, Biomimetics **4**, 62 (2019).

[26] D. C. Biggs, Nutritional ecology of *Agalma okeni* (Siphonophora: Physonectae), in *Coelenterate Ecology and Behavior*, edited by G. O. Mackie (Springer Science+Business Media, New York, 1976), pp.201–210.

[27] D. C. Biggs, Field studies of fishing, feeding, and digestion in siphonophores, Mar. Behav. Physiol. **4**, 261 (1977).

[28] K. R. Sutherland and D. Weihs, Hydrodynamic advantages of swimming by salp chains, J. R. Soc. Interface **14**, 20170298 (2017).

[29] R. J. Larson, Costs of transport for the scyphomedusa *Stomolophus meleagris* L. Agassiz, Can. J. Zool. **65**, 2690 (1987).

[30] T. Osborn and R. T. Barber, Why are large, delicate, gelatinous organisms so successful in the ocean's interior?, in *Handbook of Scaling Methods in Aquatic Ecology: Measurement, Analysis, Simulation*, edited by L. Seuront and P. G. Strutton (CRC Press, Boca Raton, 2004), pp.329–332.

[31] J. L. Acuña, A. López-Urrutia, and S. Colin, Faking giants: The evolution of high prey clearance rates in jellyfishes, Science **333**, 1627 (2011).

[32] B. J. Gemmell, J. H. Costello, S. P. Colin, C. J. Stewart, J. O. Dabiri, D. Tafti, and S. Priya, Passive energy recapture in jellyfish contributes to propulsive advantage over other metazoans, Proc. Natl. Acad. Sci. USA **110**, 17904 (2013).

[33] D. C. Hazen, *National Committee for Fluid Mechanics Films: Film Notes for Boundary-Layer Control*, Education Development Center Inc., No. 21614 (1968).

[34] R. J. Margason, Fifty years of jet in cross flow research, in *Computational and Experimental Assessment of Jets in Cross Flow*, AGARD-CP-534 (Advisory Group for Aerospace Research & Development, 1993).

[35] K. Mahesh, The interaction of jets with crossflow, Annu. Rev. Fluid Mech. **45**, 379 (2013).

[36] H. Jiang and M. A. Grosenbaugh, Numerical simulation of vortex ring formation in the presence of background flow with implications for squid propulsion, Theor. Comput. Fluid Dyn. **20**, 103 (2006).

[37] M. Sahin, K. Mohseni, and S. P. Colin, The numerical comparison of flow patterns and propulsive performances for the hydromedusae *Sarsia tubulosa* and *Aequorea victoria*, J. Exp. Biol. **212**, 2656 (2009).

[38] G. Herschlag and L. A. Miller, Reynolds number limits for jet propulsion: A numerical study of simplified jellyfish, J. Theor. Biol. **285**, 84 (2011).

[39] S. Alben, L. A. Miller, and J. Peng, Efficient kinematics for jet-propelled swimming, J. Fluid Mech. **733**, 100 (2013).

[40] S. G. Park, B. Kim, J. Lee, W.-X. Huang, and H. J. Sung, Dynamics of prolate jellyfish with a jet-based locomotion, J. Fluid. Struct. **57**, 331 (2015).

[41] A. P. Hoover, B. E. Griffith, and L. A. Miller, Quantifying performance in the medusan mechanospace with an actively swimming three-dimensional jellyfish model, J. Fluid Mech. **813**, 1112 (2017).

[42] X. Bi and Q. Zhu, Dynamics of a squid-inspired swimmer in free swimming, Bioinspir. Biomim. **15**, 016005 (2020).

[43] G. K. Batchelor, *An Introduction to Fluid Dynamics* (Cambridge University Press, Cambridge, UK, 1967).

[44] B. R. Munson, D. F. Young, T. H. Okiishi, and W. W. Huebsch, *Fundamentals of Fluid Mechanics*, 6th ed. (John Wiley & Sons, Inc., Hoboken, NJ, 2009).

[45] M. J. Lighthill, Aquatic animal propulsion of high hydromechanical efficiency, J. Fluid Mech. **44**, 265 (1970).

[46] L. E. Becker, S. A. Koehler, and H. A. Stone, On self-propulsion of micro-machines at low Reynolds number: Purcell's three-link swimmer, J. Fluid Mech. **490**, 15 (2003).

[47] A. P. Maertens, M. S. Triantafyllou, and D. K. P. Yue, Efficiency of fish propulsion, Bioinspir. Biomim. **10**, 046013 (2015).

[48] M. Tabata and K. Itakura, A precise computation of drag coefficients of a sphere, Int. J. Comput. Fluid Dyn. **9**, 303 (1998).

[49] J. O. Dabiri, S. P. Colin, and J. H. Costello, Morphological diversity of medusan lineages is constrained by animal-fluid interactions, J. Exp. Biol. **210**, 1868 (2007).

[50] J. H. Costello, S. P. Colin, and J. O. Dabiri, Medusan morphospace: Phylogenetic constraints, biomechanical solutions, and ecological consequences, Invert. Biol. **127**, 265 (2008).